

Theoretical modeling of defect segregation and space-charge formation in the BaZrO₃ (210)[001] tilt grain boundary

Anders Lindman, Edit E. Helgee, Göran Wahnström*

Department of Applied Physics, Chalmers University of Technology, SE-41296 Göteborg, Sweden

Abstract

Density-functional theory (DFT) has been used to determine the structure and interface energy of different rigid body translations (RBTs) of the (210)[001] grain boundary (GB) in BaZrO₃. There exist several different stable structures with almost equally low interfacial energy. Segregation energies of protons and oxygen vacancies have been determined for the most stable (210)[001] grain boundary structure. The results suggest that both defect species favor segregation to the same site at the boundary interface with minimum segregation energies of -1.45 eV and -1.32 eV for vacancies and protons respectively. The segregation energies have been used in a thermodynamic space-charge model to obtain equilibrium defect concentrations and space-charge potentials at a 10% dopant concentration. Space-charge potential barriers around 0.65 V were obtained at intermediate temperatures under hydrated conditions, where protons are the main contributor to the excess core charge. The potential is slightly lower under dry conditions.

Keywords: BaZrO₃, Grain boundary, Space-charge model, Density-functional theory, Defect segregation

1. Introduction

Acceptor-doped BaZrO₃ is both chemically stable and highly proton conducting and could therefore be suitable as the electrolyte material in intermediate temperature solid oxide fuel cells (SOFCs) [1, 2]. However, sintered BaZrO₃ is polycrystalline and the conductivity of that material is orders of magnitude lower due to resistance at the grain boundaries (GBs) [1, 3, 4]. Grain boundaries in BaZrO₃ do not contain secondary phases [5–8] and the high resistance is therefore considered to be an intrinsic effect.

The intrinsic blocking behavior of the grain boundaries can be described within the framework of the space-charge model. According to this model positively charged defects segregate to the grain boundary core where they give rise to an electrostatic space-charge potential. In turn, the potential depletes the surrounding regions of mobile charge carriers thus limiting the conductivity [9, 10]. The space-charge model has been applied to BaZrO₃ by several research groups where the space-charge potentials have been determined based on both experiments [6, 8, 11–16] and theoretical modeling [17–21].

For segregation to occur the defect formation energies need to be lower in the GB core. In previous work by our group we studied proton and oxygen vacancy segregation in $[\bar{1}10]$ tilt grain boundaries as well as a symmetric

(210)[001] tilt grain boundary in BaZrO₃ using density-functional theory (DFT). The results suggest that both defect species do segregate to the GB core but the strength of the segregation varied among the boundaries, favoring vacancies in some and protons in others [18, 20]. We have also studied oxygen vacancy segregation in more complex structured low-angle $[\bar{1}10]$ tilt grain boundaries using interatomic potentials, where we concluded that segregation to all considered boundaries was favorable [19]. Furthermore, Polfus *et al.* [21] have studied defect segregation to the (111) $[\bar{1}10]$ GB using DFT and their results regarding oxygen vacancy and proton segregation are in agreement with our results [20].

In this paper we extend our previous studies of grain boundaries and defect segregation in BaZrO₃ with a detailed investigation of the (210)[001] grain boundary using DFT. In order to find the most stable structures we construct an energy surface of the grain boundary by calculating the interface energy for different rigid body translations (RBT) parallel to the boundary plane. For the structure with lowest interface energy we calculate the segregation energy of oxygen vacancies and protons at different distances away from the interface. Finally, we use the defect segregation data together with a space-charge model to determine equilibrium defect concentrations and the corresponding space-charge potentials over a wide temperature range, under both dry and hydrated conditions.

*Corresponding author. Tel.: +46 (0)31 7723634

Email address: goran.wahnstrom@chalmers.se (Göran Wahnström)

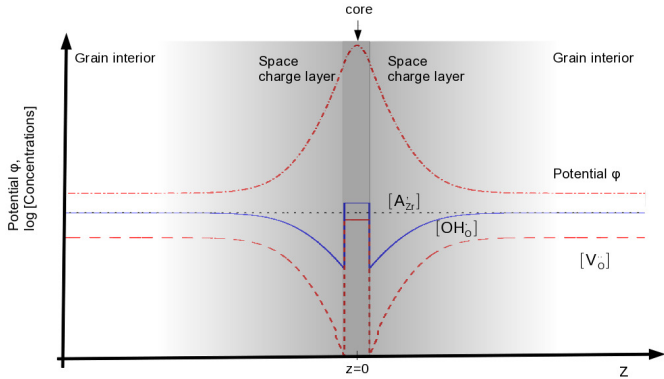


Figure 1: A schematic view of the space-charge model. The curves denoted $[A_{Zr}]$, $[OH_O]$ and $[V_O]$ corresponds to dopant, hydroxide and oxygen vacancy concentration respectively. Figure borrowed from Ref. [20].

2. Theory

To determine the distribution of defects in a material the electrochemical potential is needed. For point defects in a solid the electrochemical potential follows a Fermi-Dirac-like distribution [22]. In space-charge theory the assumption is made that the grain interior and the grain boundary are in equilibrium, i.e. the electrochemical potential is the same for both systems. The equilibrium equation that follows from this assumption together with Poisson's equation yields a set of equations from which defect concentrations and space-charge potential can be obtained.

The defects we consider in this paper are oxygen vacancies, protons (hydroxide ions) and acceptor dopants with the charge states +2, +1 and -1 respectively. We assume that the effect of other defect species, such as electron holes, is negligible. Additionally, we make use of the Mott-Schottky approximation which assumes a constant dopant concentration throughout the material. A schematic view of the space-charge model is shown in Fig. 1. A more thorough description of the space-charge theory used in this work is given in Ref. [20].

3. Computational details

3.1. Density-functional theory

The density-functional theory (DFT) calculations have been carried out using the VASP code which uses a plane wave basis set [23–26]. The generalized gradient functional due to Perdew, Burke and Ernzerhof (GGA-PBE) [27] have been employed to model exchange-correlation and the projector augmented wave method (PAW) [28, 29] was used to describe ion-electron interactions. All calculations were performed non-spin polarized with periodic boundary conditions in all directions. The plane wave cut off was 470 eV for constant volume simulations while a larger

Table 1: The unrelaxed structure dimensions and the number of atoms for the considered supercells. $a_0 = 4.25 \text{ \AA}$.

Axes	Dimensions	No. of atoms
$[\bar{1}20], [001], [210]$	$\sqrt{5}a_0 \times a_0 \times 4\sqrt{5}a_0$	100
	$\sqrt{5}a_0 \times 2a_0 \times 4\sqrt{5}a_0$	200
	$\sqrt{5}a_0 \times 3a_0 \times 4\sqrt{5}a_0$	300

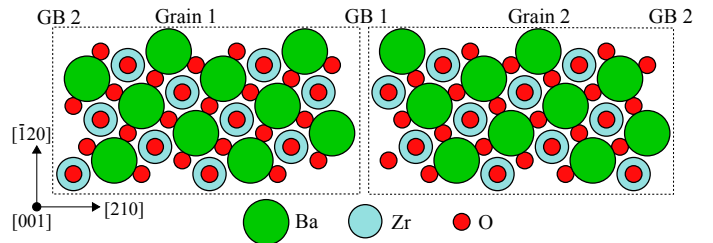


Figure 2: The initial structure for the rigid body translations (RBTs). Grain 1 was kept fixed while Grain 2 was translated in the $[120]$ and $[001]$ directions to create different structures.

value of 600 eV was used for volume relaxations. k -point sampling has been done according to the Monkhorst-Pack scheme, with a $3 \times 6 \times 1$ grid for the supercells containing 100 ions while $3 \times 3 \times 1$ and $2 \times 2 \times 1$ grids were used for the larger supercells containing 200 and 300 ions respectively. The dimensions for the different supercells are given in Table 1. The residual minimization method with direct inversion in the iterative subspace (RMM-DIIS) was used for ionic relaxation. Simulations were considered converged when the residual forces were smaller than 0.03 eV \AA^{-1} . When calculations with charged defects were performed a homogeneous background charge with the same magnitude but opposite polarity as the defect was added to make the supercell charge neutral.

3.2. γ -surface

For a given grain boundary orientation different structures can be constructed by fixing one of the grains and then translating the other one in the grain boundary plane (*c.f.* Fig. 2). This procedure will further on be referred to as a rigid body translation (RBT). To find the most stable structure of the $(210)[001]$ grain boundary several different RBTs needs to be considered.

We chose the symmetric structure given in Fig. 2 as the non-translated structure. The structure is periodic in the translational directions and we use this to define the RBTs. The notation for a RBT is (X, Y) , where X is the translation along the $[\bar{1}20]$ axis and Y is the translation along the $[001]$ axis. X and Y can take values between 0 and 1 where 0 corresponds to no translation at all and 1 corresponds to a translation of 1 periodic unit, which is the same structure as no translation at all. The length of one periodic unit is $\sqrt{5}a_0$ along the $[\bar{1}20]$ axis and a_0 along the $[001]$ axis, where a_0 is the lattice constant.

To find the most stable structures of the $(210)[001]$ grain boundary we determine the γ -surface, which is an

energy surface of the grain boundary interface. The γ -surface is constructed by calculating the grain boundary energy for different rigid body translations (RBT). The grain boundary energy is defined as

$$\gamma_{\text{gb}} = \frac{E_{\text{gb}}^{\text{tot}} - E_{\text{bulk}}^{\text{tot}}}{2A} \quad (1)$$

where $E_{\text{gb}}^{\text{tot}}$ is the energy of the grain boundary supercell, $E_{\text{bulk}}^{\text{tot}}$ is the energy of the bulk supercell and A is the area of the grain boundary interface. The factor of 1/2 is included because the grain boundary supercell contains two grain boundaries due to periodic boundary conditions (*c.f.* Fig. 2).

When relaxing the structure of different RBTs the ions are only allowed to move perpendicular to the grain boundary interface in order to keep the translation. At the same time the supercell is allowed to change size in the same direction. The change in supercell size corresponds to the grain boundary expansion which is defined as

$$\Delta_{\text{gb}} = \frac{V_{\text{gb}} - V_{\text{bulk}}}{2A} \quad (2)$$

where V_{gb} and V_{bulk} are the volumes of the grain boundary and bulk supercells.

3.3. Space-charge calculations

The space-charge calculations have been performed using a one-dimensional layer-by-layer model. This approach differs from models used in previous theoretical studies [17, 18, 21] due to that the grain boundary core is divided into layers where each layer is associated with different defect segregation energies (formation energies) as opposed to a core with only one segregation energy for each defect species. This kind of treatment is possible since we obtain layer specific segregation energies from the DFT calculations. The water partial pressure $p_{\text{H}_2\text{O}}$ was set to 0.025 bar in all calculations and the relative dielectric constant ϵ_r was chosen to be 75. For the free energy of hydration the enthalpy $\Delta H_{\text{hydr}}^{\circ} = -0.82$ eV and the entropy $\Delta S_{\text{hydr}}^{\circ} = -0.92$ meVK $^{-1}$ was chosen according to Ref. [1]. A more detailed description of this space-charge model and the implementation of it can be found in Ref. [20].

4. Results and discussion

4.1. Grain boundary structures and segregation energies

To find the most stable structures we look at low energy configurations on the γ -surface. A γ -surface has been constructed using supercells containing 100 ions, and it is shown as two curves in Fig. 3 where each curve corresponds to translations along the $[\bar{1}20]$ axis for a fixed translation in the $[001]$ direction. The γ -surface indicates that the structures which correspond to the RBTs (1/5,0), (2/5,0) and (0,1/2) are the most stable ones. Next, we consider unconstrained ionic relaxation of these three low energy structures.

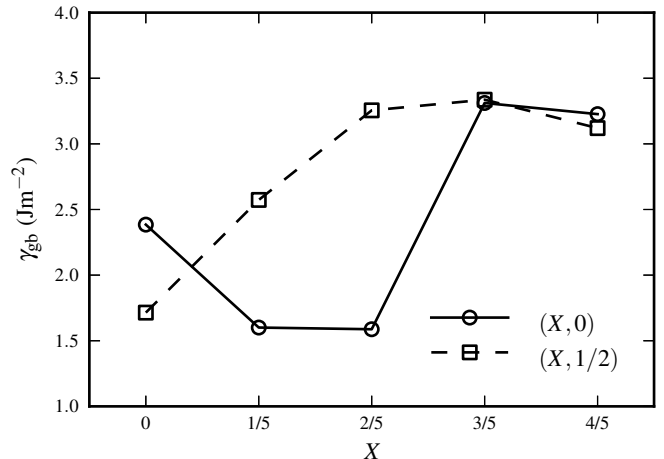


Figure 3: The grain boundary energy γ_{gb} of different rigid body translations (RBTs) (X, Y) of the $(210)[001]$ grain boundary. The x -axis corresponds to translations along the $[\bar{1}20]$ direction (X) and the different lines corresponds to translations along the $[001]$ direction (Y) (*c.f.* Fig. 2). All values are calculated using a supercell containing 100 ions where the ions only could move perpendicular to the grain boundary interface.

Table 2: Grain boundary energy γ_{gb} and expansion Δ_{gb} after unconstrained relaxation for the three most energetically favorable rigid body translations (RBT) given in Fig. 3. The RBT of the relaxed structures is also given.

RBT	RBT (Relaxed)	γ_{gb} (Jm $^{-2}$)	Δ_{gb} (Å)
(1/5,0)	(0.21,0.00)	1.22	0.95
(2/5,0)	(0.40,0.00)	1.14	0.27
(0,1/2)	(-0.01,0.50)	1.09	0.60

The grain boundary energy and expansion for the fully relaxed structures are given in Table 2. For two of the structures a slight RBT of about 0.1 Å occurred during the relaxation and these are also listed in the table. The most stable structure is the one corresponding to the RBT (0,1/2) with $\gamma_{\text{gb}} = 1.09$ Jm $^{-2}$, and the atomic structure of this grain boundary is shown in Fig. 4. This RBT has previously been found to be the most stable $(210)[001]$ structure in the perovskite SrTiO $_3$ with $\gamma_{\text{gb}} = 0.98$ Jm $^{-2}$ [30]. The (0,1/2) grain boundary will be used to study defect segregation. Furthermore, the structure corresponding to the RBT (2/5,0) is almost as stable as the (0,1/2) GB with $\gamma_{\text{gb}} = 1.14$ Jm $^{-2}$. This structure is the symmetric grain boundary which was studied previously by our group [20].

Next, we investigate if defects segregate to the (0,1/2) grain boundary. The segregation energy of a defect D is determined by

$$\Delta E_{\text{D}} = E_{\text{gb,D}}^{\text{tot}} - E_{\text{gb,D,ref}}^{\text{tot}} \quad (3)$$

where $E_{\text{gb,D}}^{\text{tot}}$ is the energy of a GB supercell with the defect and $E_{\text{gb,D,ref}}^{\text{tot}}$ is the energy of a GB supercell with the defect in the reference state. The reference state is chosen so that the defect is as far away from the grain bound-

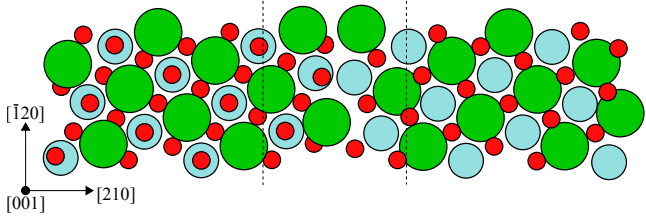


Figure 4: The atomic structure of the (210)[001](0,1/2) grain boundary. The dashed lines marks the region which is treated as the grain boundary core in the space-charge calculations. The atomic species are the same as in Fig. 2.

ary planes as possible. To reduce the possibility of the defect to interact with itself larger supercells were used. The supercell was increased by a factor of two in the [001] direction for calculations for protons and a factor of three in the same direction for oxygen vacancies.

The proton and oxygen vacancy segregation energies for the (210)[001](0,1/2) grain boundary are shown in Fig. 5. There are two segregation profiles for each defect species in the figure which corresponds to different sites on the oxygen sublattice located in the same plane. However, the even numbered planes only contain one unique site and at these planes the two profiles refer to the same oxygen vacancy or proton. To create a protonic defect is not as straightforward as creating an oxygen vacancy since the starting position has to be chosen. The most favorable proton sites in bulk BaZrO₃ has been determined in previous work [31]. Although the grain boundary is structurally different from the grain interior these bulk sites serve as suitable starting positions for our calculations. For each oxygen site we chose a few initial proton positions and the values of the proton segregation energy given in Fig. 5 corresponds to the relaxed position with lowest energy.

In Fig. 5 it can be seen that both protons and oxygen vacancies segregate to the grain boundary with minimum segregation energies of -1.45 eV and -1.32 eV for vacancies and protons, respectively. A similar vacancy segregation energy was obtained for the (112)[$\bar{1}10$] grain boundary using DFT [20], and for a set low angle [$\bar{1}10$] grain boundaries using classical interatomic potentials [19]. The proton segregation is much stronger for this grain boundary compared to structures previously studied by our group [20] and Polfus *et al.* [21] where the segregation energy is about -0.8 eV for all boundaries. Furthermore, in Fig. 5 it can also be seen that the site with lowest energy for each defect corresponds to the same oxygen site. This was also observed for the grain boundaries we considered previously [20].

When we calculate the segregation energies we either remove an oxygen ion or add a proton and then relax the structure. If there is not a local energy minimum close to the constructed defect then a substantial rearrangement of the surrounding ions can occur before the structure is relaxed. This is more likely to be a problem at the grain

boundary compared to in bulk since the grain boundary structure is less ordered. The ionic rearrangement could mean that the defect moves to a different site which means that one needs to be careful when constructing these layered segregation profiles.

For the segregation profiles in Fig. 5 this kind of rearrangement occurs at a few defect sites. The vacancy of type V¹ in plane -3 and type V² in plane 1 moved into the low energy site in plane 0 during the relaxation which means that energies of these sites does not correspond to vacancies in these planes. Furthermore, the vacancy in plane -2 and the V¹-vacancy in plane -1 corresponds to the same relaxed structure. When removing one of the oxygen ions the other one moved into a position located between the two initial sites during relaxation. For some of the protonic defects there were substantial relaxation of the surrounding ions as well resulting in protons moving to other oxygen ions. However, as mentioned previously several different starting positions were considered for each protonic defect and in the cases where a proton switched position to a different oxygen ion there were always another starting position resulting in a locally relaxed position. The values of the proton segregation energy given in Fig. 5 correspond to the proton positions with lowest energy that did not move from the initial oxygen ion.

4.2. Space-charge calculations

The space-charge simulations were performed using the defect segregation data given in Fig. 5. The segregation energies for defects located outside the planes ± 4 are all set to zero in order to reduce the computational cost, which is reasonable since the values are very small. As described in the previous section some of the oxygen vacancy segregation energies given in the figure do not correspond to vacancies in the given planes. In order to not count the same vacancy site more than once we use segregation energies obtained from unrelaxed structures in the cases where the vacancy moved significantly during relaxation. We then have $\Delta E_V = 0.12$ eV for the V¹ site in plane -3 and $\Delta E_V = 0.65$ eV for the V² site in plane 1. Moreover, the V¹ site in plane -1 and the site in plane -2 have the same structure and can thereby not be occupied simultaneously with same low segregation energy. To account for this the segregation energy of the site in plane -2 was changed to $\Delta E_V = -0.26$ eV based on unrelaxed structure calculations.

The results from the space-charge calculations obtained with a dopant concentration of 10 % can be seen in Fig. 6. The space-charge potential is about 0.65 V below 900 K under wet conditions which is consistent with experimental results [6, 8, 11–16]. Under dry conditions the potential is slightly lower by a value of 0.05–0.1 V. A similar difference in the potential barrier height between dry and wet conditions was found experimentally by Shirpour *et al.* [16]. The potential is slightly higher compared to the symmetric tilt grain boundaries studied previously by our group where a potential of about 0.6 V was found in all

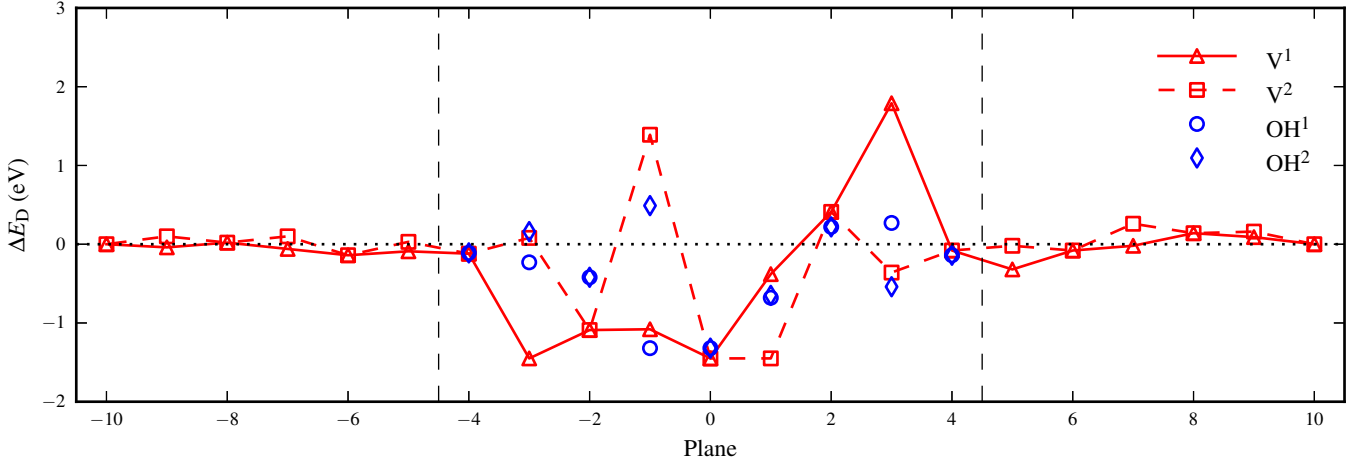


Figure 5: Oxygen vacancy and proton segregation energies of the (210)[001](0,1/2) grain boundary. The dashed lines marks the region which is treated as the grain boundary core in the space-charge calculations. The superscripts refer to different oxygen sites in the same plane for odd numbered planes while they in even numbered planes refer to the same site since those planes only contain one unique site. The planar position of each defect in the figure corresponds to the planar position of the defect prior to relaxation.

three grain boundaries under wet conditions [20]. At first, this result seems a bit odd since the proton segregation energy in the symmetric grain boundaries is -0.8 eV which is about 0.5 eV higher than the segregation energy obtained in this work and therefore should give rise to a lower potential barrier. The reason for this is that there are fewer low energy sites in this grain boundary compared to the symmetric ones.

Fig. 6 also shows that the excess core charge is only due to protons at temperatures below 900 K. This suggests that protons are the origin of the space-charge effects in this grain boundary under fuel cell operating conditions. This is consistent with the symmetric (111)[$\bar{1}10$] and (210)[001](2/5,0) grain boundaries studied in our previous work [20], where the segregation energy for protons and oxygen vacancies also is quite similar.

5. Conclusions

The (210)[001] tilt grain boundary in BaZrO_3 has been studied in terms of a γ -surface. Three different structures were found that are significantly more stable than the other structures. Proton and oxygen vacancy segregation energies have been determined for the most stable of the three structures. Both species were found to segregate to the grain boundary core, with a minimum segregation energy of -1.45 eV for vacancies and -1.32 eV for protons. Additionally, the second most stable structure is the symmetric grain boundary studied previously by our group [20].

An oxygen vacancy segregation energy of about -1.5 eV has been found in other tilt grain boundaries of BaZrO_3 [19, 20] suggesting that this is a typical value for vacancy segregation. The proton segregation tendency is found to be larger in the present study compared with some

previous investigations [20, 21], with segregation energy -1.3 eV compared with -0.8 eV in [20, 21].

Furthermore, the defect segregation energies have been used together with a 10 % uniform dopant concentration in a thermodynamic space-charge model. Potential barriers around 0.65 V were obtained at temperatures below 900 K under wet conditions, which is consistent with experimental results [6, 8, 11–16]. At these temperatures the excess core charge, and thereby the potential, is here found to be due only to protons. Furthermore, the potential barriers are slightly larger during wet conditions compared to dry ones, which also has been observed experimentally [16].

To conclude, segregation of oxygen vacancies and protons plays an important role in the formation of space-charge potentials at the grain boundary interface. Additionally, our results show that protons may be the main source of the space-charge potentials under conditions relevant for fuel cell applications.

Acknowledgments

We would like to acknowledge SNIC for computational resources and the Swedish Energy Agency for financial support.

- [1] K. D. Kreuer, *Annu. Rev. Mater. Res.* 33 (2003) 333.
- [2] E. Fabbri, L. Bi, D. Pergolesi, E. Traversa, *Adv. Mater.* 24 (2011) 195.
- [3] K. D. Kreuer, *Solid State Ionics* 125 (1999) 285.
- [4] H. G. Bohn, T. Schober, *J. Am. Ceram. Soc.* 83 (2000) 768.
- [5] F. Iguchi, T. Tsurui, N. Sata, Y. Nagao, H. Yugami, *Solid State Ionics* 180 (2009) 563.
- [6] F. Iguchi, N. Sata, H. Yugami, *J. Mater. Chem.* 20 (2010) 6265.
- [7] P. I. Dahl, H. L. Lein, Y. Yu, J. Tolchard, T. Grande, M.-A. Einarsrud, C. Kjølseth, T. Norby, R. Haugrud, *Solid State Ionics* 182 (2011) 32.
- [8] M. Shirpour, R. Merkle, J. Maier, *Solid State Ionics* 225 (2012) 304.

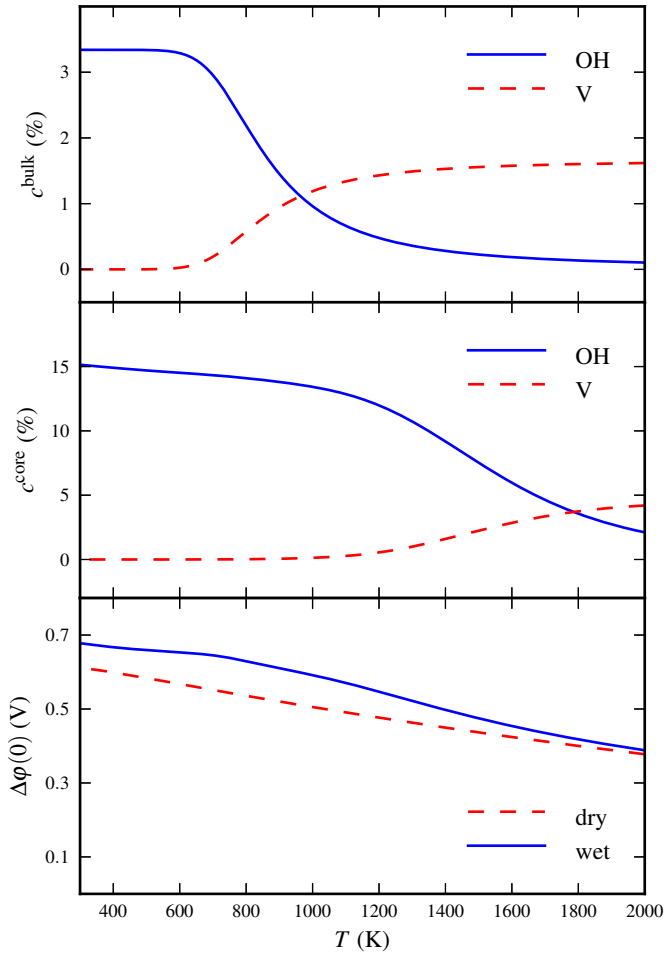


Figure 6: Results from space-charge calculations obtained using the defect segregation data in Fig. 5 together with a dopant concentration of 10%. The upper and middle figure shows the oxygen vacancy and proton concentration under wet conditions in the bulk and grain boundary core respectively while the lower shows the figure space-charge potential barrier height $\Delta\varphi(0)$ for wet and dry conditions. All calculations were performed with relative dielectric constant $\epsilon_r = 75$ and water partial pressure $p_{\text{H}_2\text{O}} = 0.025$ bar.

- [9] J. Maier, Prog. Solid State Chem. 23 (1995) 171.
- [10] R. A. De Souza, Phys. Chem. Chem. Phys. 11 (2009) 9939.
- [11] C. Kjøseth, H. Fjeld, Ø. Prytz, P. I. Dahl, C. Estournès, R. Haugsrud, T. Norby, Solid State Ionics 181 (2010) 268.
- [12] C. Chen, C. E. Danel, S. Kim, J. Mater. Chem. 21 (2011) 5435.
- [13] F. Iguchi, C. Chen, H. Yugami, S. Kim, J. Mater. Chem. 21 (2011) 16517.
- [14] M. Shirpour, R. Merkle, C. T. Lin, J. Maier, Phys. Chem. Chem. Phys. 14 (2011) 730.
- [15] M. Shirpour, B. Rahmati, W. Sigle, P. A. van Aken, R. Merkle, J. Maier, J. Phys. Chem. C 116 (2012) 2453.
- [16] M. Shirpour, R. Merkle, J. Maier, Solid State Ionics 216 (2012) 1.
- [17] R. A. De Souza, Z. A. Munir, S. Kim, M. Martin, Solid State Ionics 196 (2011) 1.
- [18] B. J. Nyman, E. E. Helgee, G. Wahnström, Appl. Phys. Lett. 100 (2012) 061903.
- [19] A. Lindman, E. E. Helgee, B. J. Nyman, G. Wahnström, Solid State Ionics 230 (2013) 27.
- [20] E. E. Helgee, A. Lindman, G. Wahnström, Fuel Cells 13 (2013) 19.
- [21] J. M. Polfus, K. Toyoura, F. Oba, I. Tanaka, R. Haugsrud, Physical Chemistry Chemical Physics 14 (2012) 12339–12346.
- [22] J. Maier, Physical Chemistry of Ionic Materials, John Wiley & Sons, Chichester, West Sussex, 2004.
- [23] G. Kresse, J. Hafner, Phys. Rev. B 47 (1993) 558.
- [24] G. Kresse, J. Hafner, Phys. Rev. B 49 (1994) 14251.
- [25] G. Kresse, J. Furthmüller, Comput. Mat. Sci. 6 (1996) 15.
- [26] G. Kresse, J. Furthmüller, Phys. Rev. B 54 (1996) 11169.
- [27] J. P. Perdew, K. Burke, M. Ernzerhof, Phys. Rev. Lett. 77 (1996) 3865.
- [28] P. E. Blöchl, Phys. Rev. B 50 (1994) 17953.
- [29] G. Kresse, D. Joubert, Phys. Rev. B 59 (1999) 1758.
- [30] H.-S. Lee, T. Mizoguchi, J. Mistui, T. Yamamoto, S.-J. L. Kang, Y. Ikuhara, Phys. Rev. B 83 (2011) 104110.
- [31] M. E. Björketun, P. G. Sundell, G. Wahnström, Faraday Discussions 134 (2007) 247.